Delft University of Technology

Clustering characteristics of gas-extraction induced seismicity in the Groningen gas field

Muntendam-Bos, A. G.

Important note
To cite this publication, please use the final published version (if applicable).
Please check the document version above.

Clustering characteristics of gas-extraction induced seismicity in the Groningen gas field

A.G. Muntendam-Bos [1,2]

[1]*Dutch State Supervision of Mines, Subsurface Department, 2492 JP The Hague, The Netherlands. E-mail: a.g.muntendam-bos@sodm.nl*
[2]*Delft University of Technology, Department of Geoscience and Engineering, 2628 CN Delft, The Netherlands*

SUMMARY

The Groningen gas field in the north of the Netherlands is one of the largest gas fields in the world. Since the early 1990s induced seismicity has been recorded. The largest magnitude event observed so far was a $M_w = 3.6$ event at the town of Huizinge in 2012. The risk posed by the induced events urged the necessity to build comprehensive seismological models capable of explaining the spatial-temporal distribution of the recorded seismicity and evaluating the regional seismic hazard and risk. The link between the occurrence of the seismicity and pressure depletion due to the production of the gas has been firmly established. However, the construction of comprehensive seismological models as well as hazard assessment is complicated by the fact that it is difficult to distinguish between induced and clustered events (events triggered by stress transfer of preceding, neighbouring events). This paper explores the contribution of clustered populations (i.e. aftershocks) to the Groningen induced seismic catalogue based on a statistical methodology in the time–space–magnitude domain. Specifically, the distributions of space–time distances between pairs of nearest-neighbour earthquakes, referred to as cluster style, is analysed. The cluster style of the Groningen induced seismicity is found to be very diffuse and characterized by a very low proportion of fore-/aftershock sequences and swarms (∼5 per cent) and a large proportion of repeater events (∼10 per cent). In contrast to human-induced seismicity in other regions, the background seismicity rate of Groningen is very low. Temporal variations in background seismicity rates can be related to changes in fault loading rates induced by gas production. Furthermore, a significant amount of independent, coincidental events (events occurring very close in time, but long distances apart) are observed. As the large gas field is fully connected, loading of the faults occurs roughly simultaneously throughout the field. Hence, the statistical probability of events occurring very close in time, but spatially far apart is significantly larger than in areas of fluid-injection induced seismicity The significant amount of repeaters and coincidental events cause an overabundance of events at intermediate time- and space-distances. This is further enhanced by the larger location errors in the catalogue increasing the estimated space-distance for non-relocated events. The diffusivity due to this overabundance of events at intermediate time- and space-distances, and the low-proportion of true fore-/aftershocks renders the statistical method used incapable of deriving a proper mode-separation value. However, this is not unique to this method. Any statistical method aimed at resolving two populations will break down if one of the populations analysed is too small. Hence, it is advisable to use caution when distinguishing fore-/aftershocks sequences or swarms for induced seismicity where the relative proportion of clustered events may be significantly lower than for tectonic events. In addition, given the small proportion of clustering and the general uncertainty in earthquake statistics, the results of this paper indicate that a distinction for earthquake risk modelling in Groningen is unnecessary.

Key words: Seismicity; Earthquakes; Foreshocks; Aftershocks; Reservoirs; Geostatistics.

1 INTRODUCTION

Over the past few decades induced seismic activity related to oil and gas activities has surged (Ellsworth 2013; Keranen *et al.* 2014; Weingarten *et al.* 2015; Atkinson *et al.* 2016; Bao & Eaton 2016). In North America this increase has been associated primarily with high-rate fluid injection of large volumes of produced salt water (Ellsworth 2013; Keranen *et al.* 2014; Weingarten *et al.* 2015), or hydraulic fracturing of low-permeable shale layers (Atkinson *et al.* 2016; Bao & Eaton 2016). Extraction of natural gas from permeable sand reservoirs is the primary cause of induced seismicity in The Netherlands (Eck *et al.* 2006; Eijs *et al.* 2006; Wees *et al.* 2014; Muntendam-Bos *et al.* 2015). Especially the large Groningen gas field in the northeast of The Netherlands has induced more than a thousand registered events with local magnitudes (M_L) ranging from below 0 to 3.6 to date.

The largest event in the Groningen gas field so far ($M_L = 3.6$) occurred on 16 August 2012 near the town of Huizinge (Dost & Kraaijpoel 2013). Although the event is too small to cause huge structural damage or loss of live, the event caused significant non-structural damage throughout the region. In an area devoid of any known natural seismicity, the shaking and damage resulted in anxiety and a great deal of public turmoil. Muntendam-Bos & Waal (2013) showed that the limiting maximum magnitude, previously established at $M_L = 3.9$ (Eck *et al.* 2006), could well be exceeded. Because of this increased probability of larger magnitude events, the assessment of the risk posed by the induced seismicity changed. This urged the necessity to build comprehensive seismological models capable of explaining the spatial-temporal distribution of the recorded seismicity and evaluating the regional seismic hazard and risk.

The link between the occurrence of the seismicity and the pressure depletion due to gas withdrawal in the field has been firmly established. At least four seismological models have been developed so far for this particular purpose. Bourne *et al.* (2014) proposed a strain-based model directly connecting reservoir compaction to seismicity. This approach was later coupled by Bourne & Oates (2017) and Bourne *et al.* (2018) with an analytical approximation of the Coulomb stresses induced by reservoir depletion. Dempsey & Suckale (2017) proposed an approach coupling Coulomb failure and fracture mechanics theory to derive induced seismicity. Very recently, Candela *et al.* (2018) implemented a Coulomb rate-and-state approach to model the non-linear spatiotemporal evolution of the Groningen induced seismicity.

The construction of comprehensive seismological models capable of explaining the spatiotemporal distribution of the recorded seismicity is complicated by the fact that it is difficult to distinguish between events induced by the underlying physical mechanism and clustered events (events triggered by stress transfer of preceding, neighbouring events). Bourne *et al.* (2018) use the Epidemic Type Aftershock Sequence (ETAS) model (Ogata 2011) to include the contribution of aftershock productivity. Though this approach can result in a model which properly matches the historically observed seismicity, the joint calibration of the seismological source and ETAS-models may mask actual limitations of the seismological source model.

Alternatively, several approaches exist to decluster the earthquake catalogue, that is performing a statistical separation into background (i.e. main shocks directly induced by gas depletion) and clustered populations (i.e. aftershocks, e.g. Hartigan & Wong 1979; Baiesi & Paczuski 2004; Ansari *et al.* 2009; Mukhopadhyay *et al.* 2010; Monem & Hashemy 2011; Benitez *et al.* 2013; Georgoulas *et al.*

2013; Martínez-Álvarez *et al.* 2015). However, the ability of performing a systematic cluster analysis is hampered by the lack of a formal definition of seismic clusters. A more comprehensive approach towards objective and robust cluster analysis was recently introduced by Zaliapin *et al.* (2008) and Zaliapin & Ben-Zion (2013, 2015, 2016).

The goal of this paper is to identify the contribution of clustered populations (i.e. aftershocks) to the Groningen induced seismic catalogue. To this end, the declustering's algorithm of Zaliapin *et al.* (2008) and Zaliapin & Ben-Zion (2013, 2015, 2016), which resolves complete triggering chains based on the relative space–time–magnitude distances introduced by Baiesi & Paczuski (2004), is used. The method separates two statistically distinct sub-populations: independent events induced by the driving underlying physical mechanism of gas extraction and clustered events, which occur much closer to each other in both space and time and, by and large, should obey the conventional definitions of aftershocks. The nearest-neighbour earthquake distances quantify the deviations of observed seismicity from a time-stationary, space-inhomogeneous Poisson process. A basic assumption of the method is the feasibility to distinguish events induced by the principal physical mechanism of (differential) compaction and events induced by dynamic stress transfer during an earthquake enhancing this static stress, hence basically moving the occurrence of the event forward in time. However, whether such a clear distinction exists for relatively small induced seismic events is part of the analysis. In addition, the effect of changes in seismicity rate as well as earthquake location errors on the derived clustering and background rates are investigated in the analyses presented in this paper.

The paper is structured as follows. Section 2 describes the Groningen gas field and the data used. Section 3 summarizes the key aspects of the nearest-neighbour cluster technique used. In Section 4, the results for the Groningen induced seismicity catalogue are presented. In addition, the influence of changes in seismicity rate and earthquake location errors are assessed and an in depth analysis of some individual clusters derived by the method is presented. Finally, a discussion of the results is provided in Section 5.

2 THE GRONINGEN GAS FIELD

2.1 Tectonic framework

The Groningen reservoir is located at a depth of approximately 3 km within the Rotliegend sandstone. The sands and gravels comprising the Upper Permian Rotliegend sediments were deposited in a broad basin stretching from the United Kingdom in the west to Poland in the east. The sands were deposited on top of the Base Permian unconformity. The gas generating Carboniferous rocks are located directly underneath this unconformity. The reservoir overburden consists of a thick layer of Zechstein halite and anhydrite salt deposits. The reservoir and overburden sequences were deposited under tectonically very quiescent conditions.

Within the reservoir over 1100 normal (extensional) faults have been mapped. The main fault trend is NNW–SSE, though also E–W and N–S trending faults have been identified. The highest density of faults is in the southern sector of the reservoir. It is generally accepted that most of the faulting on the reservoir faults occurred during the Late Jurassic to Early Cretaceous rifting phase. The final phase of tectonic activity in the Groningen area was the Late Cretaceous to Early Tertiary inversion which resulted in thinning of the upper part of the Paleogene over Groningen.

Over geological time, the Zechstein salt layer has changed thickness due to the movement of salt into salt domes and salt walls at the eastern and western boundaries of the field. All reservoir faults terminate in the anelastic Zechstein overburden as the salt layer effectively decouples subsalt faults from supra-salt faults (Visser & Solano Viota 2017).

2.2 Production history

The Groningen gas field (Fig. 1a) was discovered in 1959. The field has an estimated total volume of gas of over 2800 billion cubic metre (bcm, Waal *et al.* 2015). Production from the field commenced in 1963 and offtake rates increased rapidly until the mid-1970s (Fig. 1b). Following the oil crisis, rates decreased significantly in order to conserve gas reserves. In response to increasing market demand and decreasing offtake from the small Dutch gas fields, rates increased again between 2000 and 2014. Following the study of Muntendam-Bos & Waal (2013) production offtake was decreased gradually in five consecutive steps from a production of 54 bcm a^{-1} in 2013 to 21.6 bcm a^{-1} in April 2017. Following the $M_L = 3.4$ event near Zeerijp on 8 January 2018, the Dutch government decided to further reduce gas production over the coming years aiming at a complete termination of production in 2030.

2.3 Observed seismicity

The first earthquake in the Groningen gas field was registered in December 1991 (Fig. 1c). A regional network to monitor the induced seismicity was built and became operational in 1995 (Dost & Haak 2007). This network consisted of eight stations at which three-component geophones were deployed at four depth levels in shallow (200–300 m deep) boreholes. The network was designed to be complete in terms of both detection and location thresholds for earthquakes of magnitudes of 1.5 and above (Dost & Haak 2007). The actual location threshold of the network is $M_L \sim 1.0$–1.5. Recent analysis by Paleja & Bierman (2016) and Dost *et al.* (2017) determined that the magnitude of completeness of the KNMI catalogue was $M_c \sim 1.2$ between 2003 and 2010. Prior to 2003 sufficient data is lacking to establish the magnitude of completeness (Paleja & Bierman 2016). However, as the network was not altered between 1995 and 2010, it is reasonable to assume this magnitude of completeness is also valid for the period between 1995 and 2003. In 2010 the network was extended by three stations in order to increase the aperture of the network (Dost *et al.* 2017). This extension of the network lowered the magnitude of completeness to $M_c \sim 0.9$ (Paleja & Bierman 2016; Dost *et al.* 2017). A recent very significant improvement of the seismic network in 2014 has further reduced the magnitude of completeness of the catalogue to $M_c \sim 0.5$ (Paleja & Bierman 2016; Dost *et al.* 2017). In order to ensure a reasonably uniform quality of the catalogue, in this paper all data prior to 1 January 1995 are excluded and a M_c of 1.2 is adopted.

The KNMI Groningen network epicentre resolution was 0.5–1.0 km (Dost *et al.* 2017). However, due to the sparseness of the network, the depth resolution is very limited. In practice, the depth of the event hypocentre in the Groningen KNMI catalogue is assumed to be 3 km, coinciding with the depth of the Groningen reservoir layer. The extension of the seismic network in 2014 allowed for actual hypocentre locations to be derived (Spetzler & Dost 2017; Willacy *et al.* 2019). Both studies observe that most induced earthquakes are indeed located within the reservoir layer showing a strong correlation between the earthquake location and the major

NNE–SSE trending faults. Willacy *et al.* (2019) also derived focal mechanisms for the 100 events assessed. The results show clear consistent normal faulting mechanisms, in some cases associated with some oblique motion.

Initially, seismic activity was limited and located at the centre of the field. However, after a decade of reasonably constant rates, seismic activity increased exponentially between 2003 and 2013 (Fig. 1c; Bourne *et al.* 2014; Nepveu *et al.* 2016). Following the production rate reduction in 2014 a fast response of the seismicity rate is observed (e.g. Waal *et al.* 2015; Nepveu *et al.* 2016; Muntendam-Bos *et al.* 2017). However, despite the reduction in seismicity rate observed, larger magnitude events still occur (e.g. the $M_L = 3.4$ event at Zeerijp on 8 January 2018 and the $M_L = 3.4$ event at Westerwijtwerd on 22 May 2019).

3 EARTHQUAKE NEAREST NEIGHBOURS METHODOLOGY

The earthquake nearest neighbour (ENN) approach of Zaliapin *et al.* (2008) commences with the time–space–magnitude distance between earthquakes introduced by Baiesi & Paczuski (2004). For any two earthquakes in a catalogue that is characterized by occurrence time $\{t_i\}_{i=1,...,N}$, hypocentre $(x_i, y_i, d_i)_{i=1,...,N}$ and magnitude $\{m_i\}_{i=1,...,N}$ this distance is defined as

$$\eta_{ij} = \begin{cases} t_{ij} r_{ij}^f 10^{-bm_i}, & t_{ij} > 0 \\ \infty, & t_{ij} \le 0, \end{cases} \quad (1)$$

where $t_{ij} = t_j - t_i$ is the event intercurrence time, which is positive if event j occurred after event i; $r_{ij} > 0$ is the spatial distance between the earthquake hypocentres; f is the (fractal) dimension of the hypocentres; and b is the b-value of the Gutenberg–Richter law (Gutenberg & Richter 1944, 1954). The *nearest neighbour* distance is defined as $\eta_j^* = min_i \eta_{ij}$ and event i is called the parent of event j.

The time- and space-distances between event j and its parent i normalized by the magnitude of the parent event are defined as

$$T_{ij} = t_{ij} \, 10^{-qbm_i}; \quad R_{ij} = r_{ij}^f \, 10^{-pbm_i}; \quad p + q = 1. \quad (2)$$

The normalization of the original times t and distances r to the parent by the magnitude of the parent event ensures that the cloud of events corresponding to parent events of different magnitudes closely overlap. This normalization ensures the offspring of larger magnitude events spread wider in space and longer in time than the offspring of smaller magnitude events.

In this definition $\log_{10}(\eta_{ij}) = \log_{10}(T_{ij}) + \log_{10}(R_{ij})$. In case of a time-stationary, space-inhomogeneous Poisson process with a Gutenberg–Richter magnitude distribution a unimodal distribution of $(\log T, \log R)$ is obtained which is concentrated along the line $\log_{10}(T_{ij}) + \log_{10}(R_{ij}) =$ constant (Zaliapin *et al.* 2008). A typical ETAS aftershock model has two prominent modes: one corresponding to the background time-stationary, space-inhomogeneous Poisson process and a second consisting of events located considerably closer to its parents in time and space. This second mode is representative for the aftershock sequences (Zaliapin *et al.* 2008). Our analysis focuses on possible deviations from these distributions in the extraction induced seismicity of the Groningen gas field.

In this paper, we use epicentres rather than hypocentres because the depth coordinates of the events have been fixed at 3 km depth in the earthquake catalogue used. In the computation of distances η, T and R we use $b = 1$, $f = 1.6$ and $p = 0.5$. Zaliapin & Ben-Zion (2013) showed that the derived cluster structure is fairly
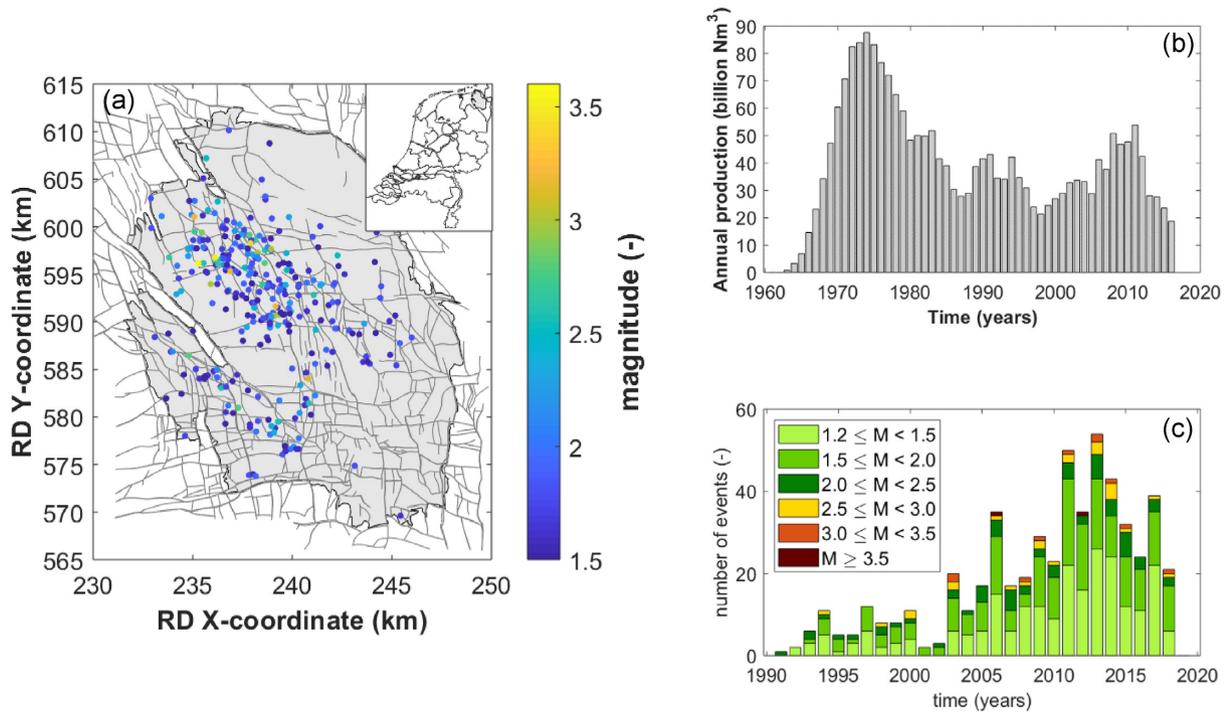
Figure 1. (a) The Groningen gas field on a map of the region and its seismicity ($M_l \geq 1.5$) as reported by the Royal Dutch Metrological Institute (KNMI). The colour coding of the seismicity indicates the local magnitude (–) of the events. (b) The annual volumes of gas produced from the Groningen gas field since the onset of production in 1964. (c) The development of the Groningen seismicity with time. The colour bars denote the annual number of earthquakes in different magnitude classes.

robust with respect to these parameters. For the Groningen field, this is confirmed by the sensitivity analysis provided in the electronic supplement to this paper.

4 RESULTS

4.1 Cluster style of Groningen induced seismicity

Fig. 2 shows the 2-D distribution of the rescaled time (T) and rescaled distance (R) to the parent for seismic events of $M_L \geq 1.2$ within the Groningen gas field in the period 1995–2019. Each point in Fig. 2(a) corresponds to a catalogue event and provides information on the time- and space-distance to its parent. The background mode and mode separation value are estimated by using a 1-D Gaussian mixture model (Hicks 2011), where $\log_{10} \eta_b = \text{mean}(\log_{10} \eta_{ij})$ is taken over all the background events. A 2-D Gaussian mixture model estimate provides identical results.

The background mode for Groningen ($\log_{10} \eta_b = -2.5$) is located quite far from the origin, indicating a relatively low seismicity rate. However, the background rate is slightly higher than the background rate derived for a time-stationary, space-inhomogeneous Poisson process ($\log_{10} \eta_b = -2.2$; Fig. 2b). This is closely related to the much broader distribution of the nearest neighbour distances. The proportion of events in the background mode is very high (Fig. 2). In addition, there is a number of events occurring in the lower-right corner of the *(T,R)*-plane. These events occur at very short distances from their parent, but at times significantly exceeding the duration of a typical aftershock sequence. These events are known as repeaters (Zaliapin & Ben Zion 2016).

The mode separation value is generally found to be located at $\mu_0 \approx 10^{-5}$–10^{-6} (Zaliapin *et al.* 2008; Zaliapin & Ben-Zion 2013,

2015). No events are predicted to occur below $\mu_0 \approx 10^{-5}$ in a time-stationary, space-inhomogeneous Poisson process (Fig. 2b; Zaliapin *et al.* 2008; Zaliapin & Ben-Zion 2013). Hence, aftershock events are expected to occur at nearest neighbour distances $\mu_0 < 10^{-5}$ (Zaliapin *et al.* 2008; Zaliapin & Ben-Zion 2013, 2015). In the Groningen induced seismicity catalogue the number of these typical aftershocks in the catalogue is, with 3 per cent, very limited (Table 1). The aftershocks occur at very short normalized times ($T \approx 10^{-5}$) from their parents but at relatively large normalized distances ($R \approx 10^{-1} - 10^{-2}$).

The clustering style for Groningen lacks a clear separation between the background and clustered events. The bimodal distribution of ($\log T$, $\log R$) observed in other earthquake catalogues and for a typical ETAS aftershock sequence (see fig. 2 of Zaliapin *et al.* 2008) is actually not present in the histogram of Fig. 2(b). The Gaussian mixture model derives a relatively high mode separation value of $\mu_0 = 10^{-4.23}$. This is most likely due to the absence of a clear clustered-events-mode. The general behaviour of the Groningen seismicity seems diffuse with a slight overabundance of events located between $\log_{10} \eta = -3$ and $\log_{10} \eta = -5$ compared to the unimodal distribution of a time-stationary, space-inhomogeneous Poisson process (Fig. 2b). In contrast to the typical aftershocks, the events in this realm occur over a very broad range of normalized inter-event distances ($R \approx 10^{-3} - 10^{1}$).

4.2 Spanning network, forest of earthquakes

The single cluster containing all the nearest neighbour links between each examined event *j* and its parent *i* form a spanning network. The structure of the spanning network is a tree, which means it does not have loops. The spanning network for the Groningen induced
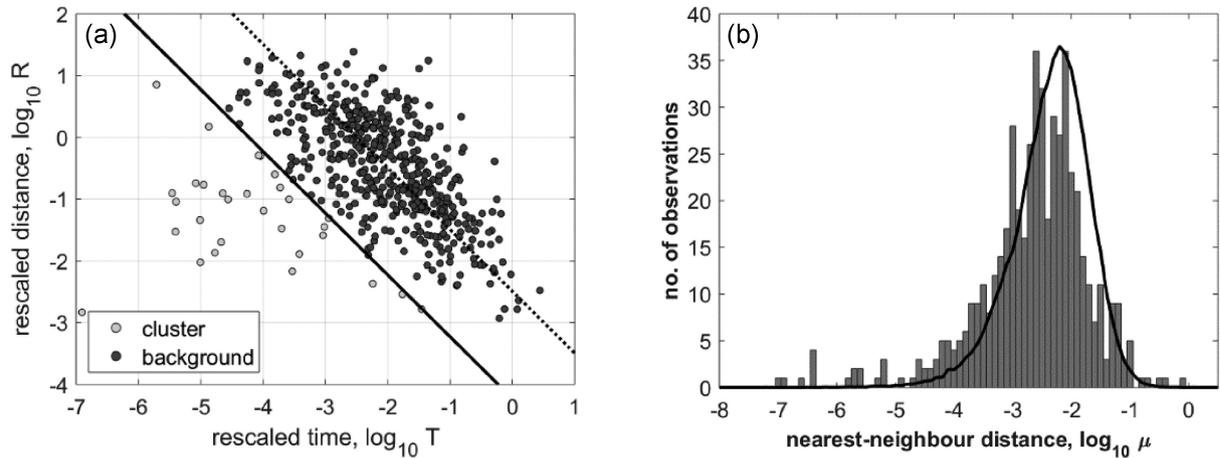
Figure 2. (a) Clustering style of seismicity in the Groningen gas field. The panel shows the 2-D distribution of the rescaled time (*T*) and rescaled distance (*R*) to the parent for the Groningen gas field in the period 1995–10/2018. The solid diagonal line denotes the derived mode separation threshold, $\log_{10} \eta_0$, and the dashed diagonal line denotes the background location, $\log_{10}\eta_B$ (also reported in Table 1). (b) Histogram of the nearest-neighbour distances $\log 10\eta_{ij}$ for the Groningen seismicity catalogue. The solid line shows the mean of 100 realizations for a time-stationary, space-inhomogeneous Poisson process with exponential magnitudes. The number of events and the inhomogeneous spatial distribution corresponds to the number of events and inhomogeneous spatial distribution of the Groningen seismicity catalogue.

Table 1. Basic characteristics of background and cluster populations for the full period and four subperiods.

Time period	Mode separation threshold, $\log_{10} \eta_0$[a]	Background proportion, P_B	Background location, $\log_{10} \eta_B$	Cluster proportion, $P_C = 1-P_B$	Background/cluster proportion assuming $\log_{10} \eta_0 = -5$
Full period: 1/1995–1/2019	−4.23	0.94	−2.49	0.06	0.97/0.03
1/1995–1/2003	−2.05	0.74	−1.36	0.26	100/0.00
1/2003–1/2011	−4.30	0.96	−2.53	0.05	0.96/0.04
1/2011–5/2014	−4.16	0.92	−2.62	0.08	0.97/0.03
5/2014–1/2019	−3.14	0.78	−2.31	0.22	0.96/0.04

[a]Estimated using the 1-D Gaussian mixture model (Hicks 2011).

seismicity catalogue is shown in Fig. 3(a). Each link in the tree can be assigned a strength, which is inversely proportional to its nearest neighbour distance μ. The mode separation threshold now differentiates between the weak links (μ > μ₀) and the strong links (μ ≤ μ₀). By removing the weak links from the spanning network, a spanning forest of trees is obtained (Fig. 3b). The majority of the trees in the forest (90 per cent) consist of only a single event, which are indicated by grey dots. The multi-event trees (indicated by the larger black dots and connecting lines) are called families.

Most families in Fig. 3(b) consist of events which are closely clustered in time and space. However, a couple of families are observed of which the events occur very close to each other in time, but are located quite far apart spatially. This is consistent with the events observed in the upper-right corner of Fig. 2(a). In this paper, these events will be referred to as coincidental events.

4.3 Events at intermediate nearest neighbour distances

A slight overabundance of events at intermediate nearest neighbour distances ($\log_{10}\eta_0 = -3$ and $\log_{10}\eta_0 = -5$) is observed. Fig. 3c shows the spanning forest derived by removing only the very weak links: $\log_{10}\eta_0 > -3$ thus allowing for an analysis of possible families in this intermediate realm. The majority of the families occur from 2003 onwards. Fig. 3(c) clearly shows the presence of (1) families which occur very close in space, but over long time-periods, so called repeaters; (2) families of which the events occur very close

to each other in time, but are located quite far apart spatially, the co-incidental events and (3) families of events located relatively close in both space and time (true aftershocks).

To further emphasize the differences between the families, the nearest neighbour forest of events located within a single rupture distance from the parent is derived. The rupture length is estimated using the model of Leonard (2010, 2012) for small magnitude events ($M \leq 4$) which has been derived for events in interplate and stable continental regions:

$$\log_{10} L_{\mathrm{rup}} = \frac{d * M + c - 6.1}{3.0} + \varepsilon\sigma, \tag{3}$$

where $d = 1.5$ and $c = 9.1$ are the parameters relating earthquake magnitude (*M*) to seismic moment, $\sigma = 0.19$ is the uncertainty in the rupture length estimate and $\varepsilon = 2.45$, which results in a derived rupture length which corresponds to the upper 95 per cent confidence limit. Here, the 95 per cent confidence limit is explicitly used in part to account for location uncertainties in the data, as well as for the fact that not the distance to the rupture of the parent, but the coulomb stress changes induced by the parent is responsible for triggering aftershocks and these significantly exceed the rupture area (King *et al.* 1994; Harris 1998; Stein 1999; Freed 2005; Toda *et al.* 2011).

Fig. 3(d) shows there is an abundance of repeaters in the seismic catalogue. Several locations where larger magnitude events occur ($M \geq 3.0$; indicated by the stars) have experienced seismicity prior to the larger events or experience more seismicity at a later stage.
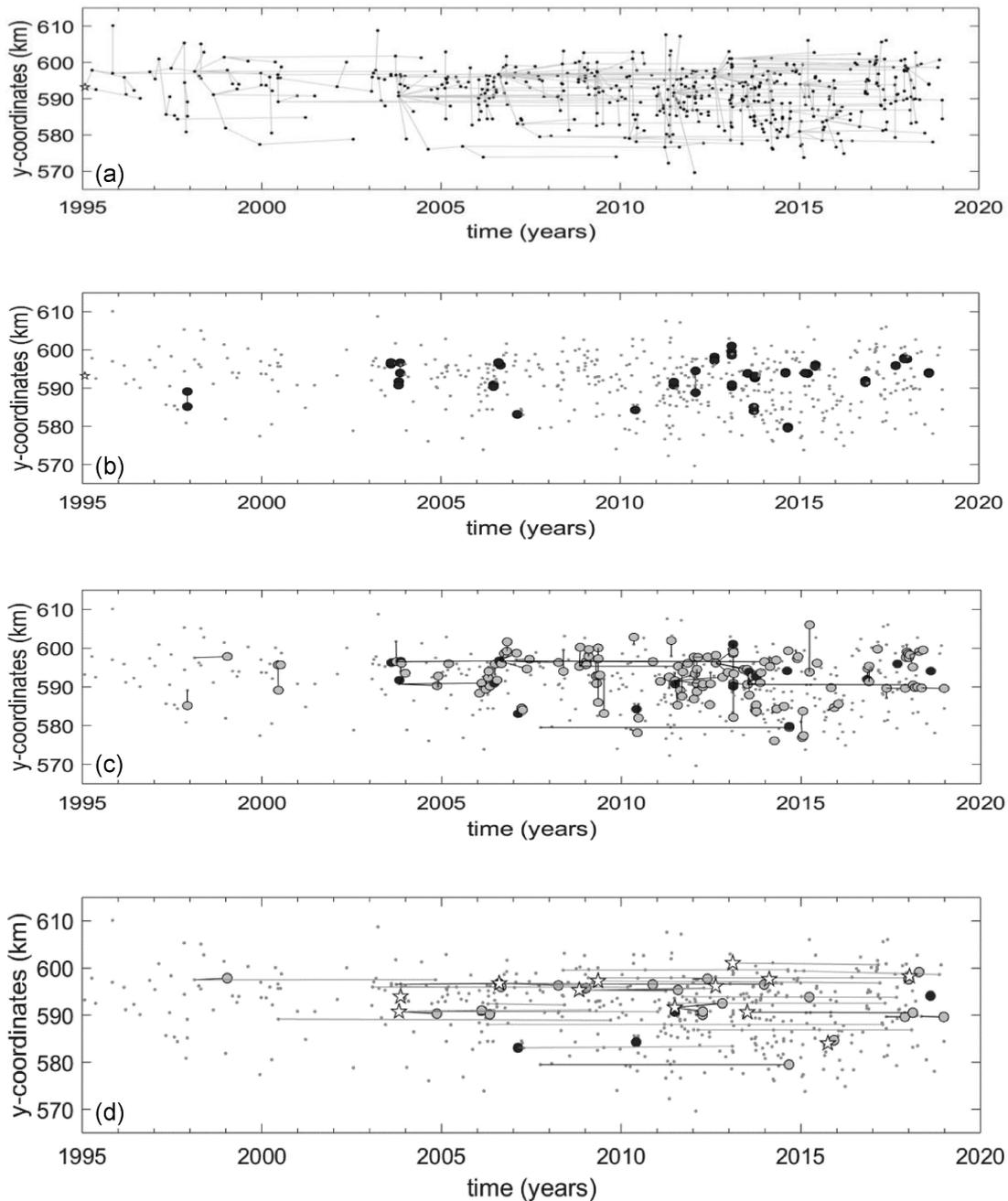
Figure 3. (a) Spanning network for the nearest-neighbour analysis of earthquakes in the Groningen induced seismicity catalogue. The nearest neighbour links are indicated by grey lines. (b) Nearest neighbour forest derived by removing the weak links ($\mu > \mu_0$) from the spanning network. (c) Nearest neighbour forest derived by removing the links ($\mu > -3$) from the spanning network. The light grey circles indicate the events with $-5 \leq \log_{10}\eta \leq -3$. The black circles indicate the events with $\log_{10}\eta \leq -5$. (d) Nearest neighbour forest for events located within one rupture length of its parent. The stars denote the events of $M \geq 3.0$. The light grey circles indicate the events with $-5 \leq \log_{10}\eta \leq -3$. The black circles indicate the events with $\log_{10}\eta \leq -5$.

The true fore-/aftershock or cluster activity, with $\log_{10}\eta_0 \leq -5$, is limited to a single aftershock sequence and three clusters of events containing a total of only seven events.

4.4 Temporal development of Groningen induced seismicity cluster style

The validity of these observations requires some scrutiny. The ENN-methodology assumes a time-stationary, space-inhomogeneous Poisson process for the background seismicity (Zaliapin *et al.* 2008;

Zaliapin & Ben-Zion 2016). For induced seismicity, changes in seismicity rate are common. Hence, changes in rate may hamper a comprehensible interpretation of the cluster style for the full time-period.

As discussed above, the seismic activity in the Groningen gas field has not been time-stationary. A temporal non-stationary Poisson process can be modelled in finite samples as a piece-wise stationary processes. Based on the Bayesian Change Point analysis of Sijacic *et al.* (2017), four periods with relatively stationary seismicity rates can be selected and analysed independently (Table 2).

Table 2. Basic characteristics of background and cluster populations for the KNMI and relocated catalogue (Willacy *et al.* 2019) for the time period 2015–2019.

Catalogue	Mode separation threshold, $\log_{10} \eta_0{}^*$	Background proportion, P_B	Background location, $\log_{10} \eta_B$	Cluster proportion, $P_C = 1 - P_B$	Background/cluster proportion assuming $\log_{10}\eta_0 = -5$
KNMI	−3.34	0.81	−2.32	0.19	0.97/0.03
Willacy *et al.* (2019)	−3.36	0.79	−2.32	0.21	0.96/0.04

The cluster styles of the four periods are given in Fig. 4. The background mode ($\log_{10} \eta_B$; Table 2) is initially very low. This is consistent with an average event rate in the period from 1995–2003 of ∼10 events of $M_L \geq 1.2$ per year. This period also appears to contain a large proportion of clustered events (Table 1). However, the derivation of the mode separation value is significantly hampered by the limited data set. In fact, the two modes are found to overlap. Subsequently, clustered events are also erroneously found at the opposite site of the background events at large rescaled times and distances. Based on a typical mode separation value of $\mu_0 \approx 10^{-5}$ no true fore/aftershock or clustered events are determined in this time period (Table 1). This is confirmed by the nearest neighbour forest of events within a rupture distance for this time period (Fig. S2 in the electronic supplement), which shows only a single repeater and no fore/aftershock or clustered events. Hence, the Gaussian mixture model attempts to derive a separate cluster mode which is actually absent. Imposing a single mode on the data for this period results in a background mode of $\log_{10} \eta_B = -1.68$.

In the following two periods, the background mode shows a decrease. The lowest background mode of $\log_{10}\eta_B = -2.62$ is obtained for the third period. This decrease in background mode indicates a clear increase in seismicity rate over these two periods. This is consistent with the observed increase in seismicity (Fig. 1c; Muntendam-Bos & Waal 2013; Bourne *et al.* 2014; Nepveu *et al.* 2016; Muntendam-bos *et al.* 2017; Sijacic *et al.* 2017). The aftershock proportion in the second and third period is very low and close to the true fore-/aftershock proportions derived (Table 1).

The fourth time period obtains a higher background mode indicating a slight reduction in seismicity rate which is consistent with derived decreases in seismicity rate as production from the field was reduced (De Waal *et al.* 2015; Nepveu *et al.* 2016; Muntendam-Bos *et al.* 2017; Sijacic *et al.* 2017). For the final period a quite high mode separation value is obtained, resulting in a significant proportion of apparent clustered events. In contrast, the proportion of true fore/aftershock events is found to be very consistent to the proportion found in the second and third period. The high model separation value seems to be driven by the appearance of a small second mode between $\log_{10}\eta_0 = -3$ and $\log_{10}\eta_0 = -5$ (Fig. S6 of the electronic supplement). In fact, the histograms of the nearest-neighbour distances $\log_{10}\eta_{ij}$ for the second till fourth time periods (Fig. S6) all show the abundance of events between $\log_{10}\eta_0 = -3$ and $\log_{10}\eta_0 = -5$ which was also observed for the full period.

The temporal analysis clearly derives the trend in changing background seismicity rate observed in the Bayesian Change Point analysis of Sijacic *et al.* (2017). Except for the initial period, when true fore-/aftershocks are completely absent in the data, the proportion of true fore-/aftershocks remains remarkably constant. If compared to the number of stronger events ($M \geq 2.5$) in the four periods (3, 13, 10 and 9, respectively), this could indicate the system is getting more susceptive for the generation of fore-/aftershocks. This would imply that either events of these magnitudes would be becoming increasingly capable of generating clustered events or the larger magnitude events could be associated with increasing numbers of fore-/aftershocks.

4.5 Influence of location errors

Any clustering analysis needs to be conscience of the influence of catalogue uncertainties, particularly event location errors, on the cluster model results. Zaliapin & Ben-Zion (2015) documented three major artefacts large location errors could induce: (1) derivation of an increased distance between parent and offspring, (2) an underestimation of clustering and (3) an overestimation of background rates.

The horizontal resolution of the events in the Groningen catalogue is on the order of 0.5–1 km (see also Section 2.3; Dost *et al.* 2017). However, several relocation studies have shown horizontal shifts of event locations by several kilometres (Spetzler & Dost 2017; Willacy *et al.* 2019). This could significantly influence the interpretation of the cluster model results. By applying full-waveform inversion, Willacy *et al.* (2019) were able to derive much more accurate event locations for 100 events between January 2015 and September 2017. Since, the study has become a continuous effort further relocating 30 events in 2017 and 66 events in 2018. The errors in the derived locations are on the order of 50–100 m. Note that for the non-relocated events in the time-period 2015–2019 the relocated catalogue retains the original KNMI-locations.

The ENN-analysis for the relocated catalogue of Willacy *et al.* (2019) is compared to the results of the main Groningen catalogue for the time-period January 2015 till January 2019. In this period the magnitude of completeness of the network was $M_c = 0.5$ (Paleja & Bierman 2016; Dost *et al.* 2017). In order to retain a significant catalogue, all events with $M_L \geq 0.5$ have been adopted in this comparison. The results for both catalogues are shown in Fig. 5.

The reduction of the location errors in the Groningen catalogue leads to a significant reduction in rescaled distance of the clustered events (Fig. 5) and to more pronounced clustering (Fig. 6). The proportion of true fore-/aftershock sequences or true clustering is 1 per cent larger in the relocated catalogue compared to the original catalogue. However, as relocation was not feasible for all events, even within the relocated catalogue the events with larger location uncertainties still hamper interpretation of the analysis. It is probable that the proportion of true fore-/aftershock is somewhat underestimated.

4.6 Individual cluster characteristics

By analysing individual clusters some of the specific characteristics of the clusters and the possible overabundance of events between $\log_{10}\eta = -3$ and $\log_{10}\eta = -5$ can be investigated in more detail. In order to minimize the impact of location errors on the analysis, the relocated data set between January 2015 and January 2019 is used. Three specific families of events are investigated: the sequences associated with the two largest events (the *M* 3.1 Hellum and the *M* 3.4 Zeerijp earthquakes) and the Wirdum/Loppersum sequence late 2016, early 2017. A detailed description of these three sequences is provided in the electronic supplement to this article.

According to the ENN-procedure all three sequences contain both clustered, coincidental and repeater events. However, close inspection of the results show that the number of true fore-/aftershocks
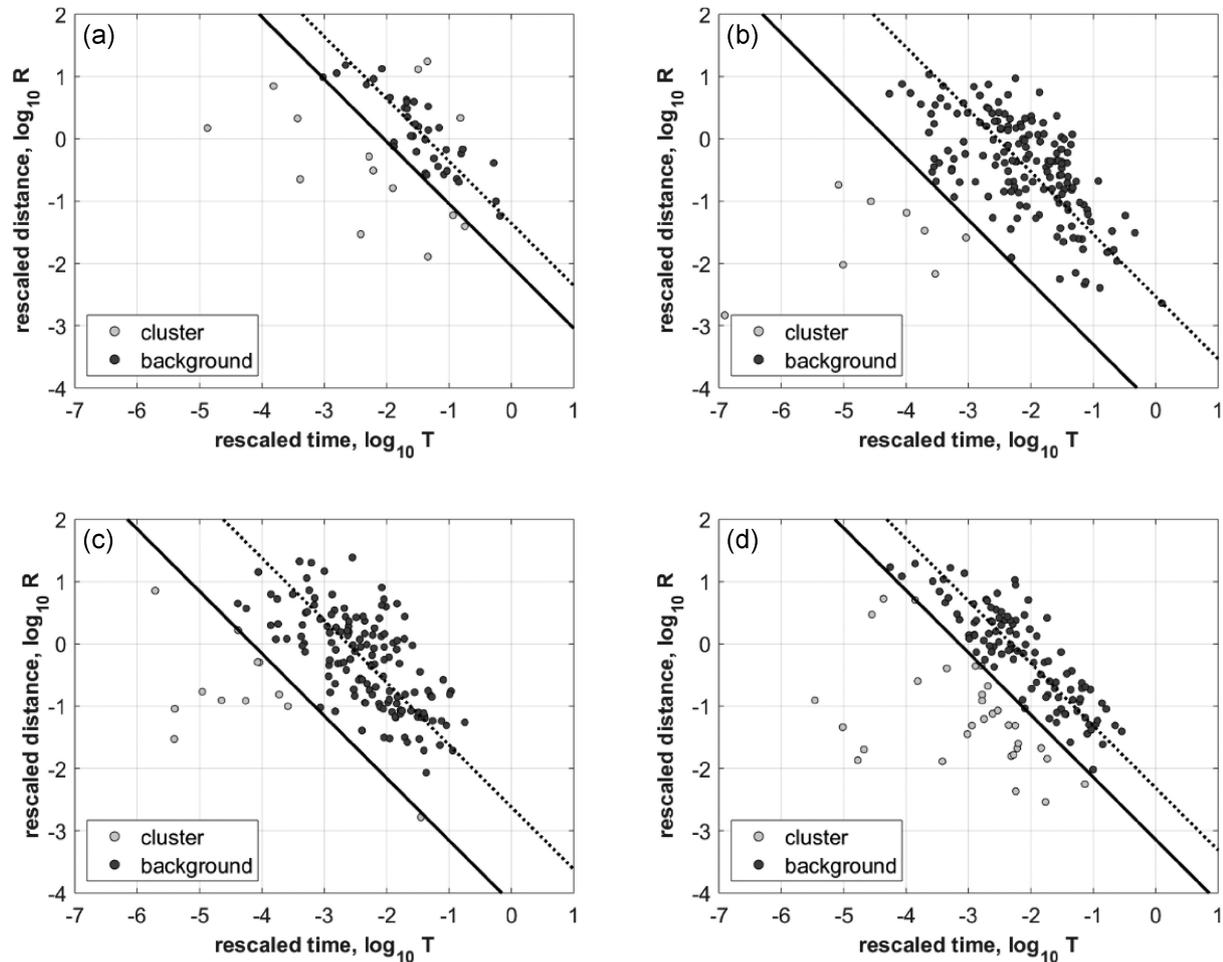
Figure 4. Clustering style of seismicity in the Groningen gas field. Each panel shows the 2-D distribution of the rescaled time (T) and rescaled distance (R) to the parent for the Groningen gas field for the time periods (a) 1995–2003, (b) 2003–2011, (c) 2011–5/2014 and (d) 5/2014–2019.

or true clustered events is very low. Most of the events actually are repeater and coincidental events.

The Hellum M_L 3.1 earthquake should be considered a relatively larger magnitude earthquake exempt of any fore- or aftershock events. In contrast, the M_L 3.4 Zeerijp earthquake was preceded by a single foreshock and induced one clear aftershock. The three other events preceding the Zeerijp event should be considered independent, coincidental events occurring on near-by critically stressed fault traces with similar strikes which were activated roughly at the same time.

Apart from clear fore-/aftershock sequences such as Zeerijp, Groningen induced seismicity also shows clusters of only small events. Hence, the proportion of true clustered events is not driven solely by the presence of larger magnitude events.

5 DISCUSSION AND CONCLUSIONS

5.1 Clustering of extraction versus injection and mining induced seismicity

The clustering characteristics of human-induced seismicity were previously studied by Zaliapin & Ben-Zion (2016). Their study focused on The Geysers, the Coso and Salton Sea geothermal fields in California and the TauTona gold mine in South Africa. They concluded induced seismicity distinguishes itself from regular tectonic

activity by having (1) a higher rate of background events, (2) a faster temporal offspring decay, (3) a higher rate of repeating events, (4) a larger proportion of small clusters and (5) a larger spatial separation between parent and offspring. For the Coso geothermal field, an increased background rate and higher rate of repeating events was also identified by Schoenball *et al.* (2015). Llenos & Michael (2013, 2016) derived higher background rates and increased aftershock productivity in regions experiencing significantly increased pore pressures due to fluid injection.

The main difference between Groningen and these regions of human-induced seismicity is the very low rate of background seismicity found for Groningen and more or less absence of aftershock productivity. The difference in background seismicity rate can be explained by the difference in basic geomechanical processes inducing injection and production induced seismicity.

The principle of effective stress (Terzaghi 1923) allows for the evaluation of failure on a fault zone neglecting the deformation of the rock. For injection induced seismicity, the increase in pressure leads to a decrease of effective stress in a fault or fracture shifting the Mohr–Coulomb circle towards failure (Given that ΔP is positive for injection and assuming compressive stresses positive in an extensive stress regime, which is consistent with the tectonic setting of the faults in the Groningen gas field and the focal mechanisms of the induced seismic events (see also Section 2); Fig. 7(a). Similarly, the decrease in pressure due to production leads to an increase of effective stress and stabilization of the faults.
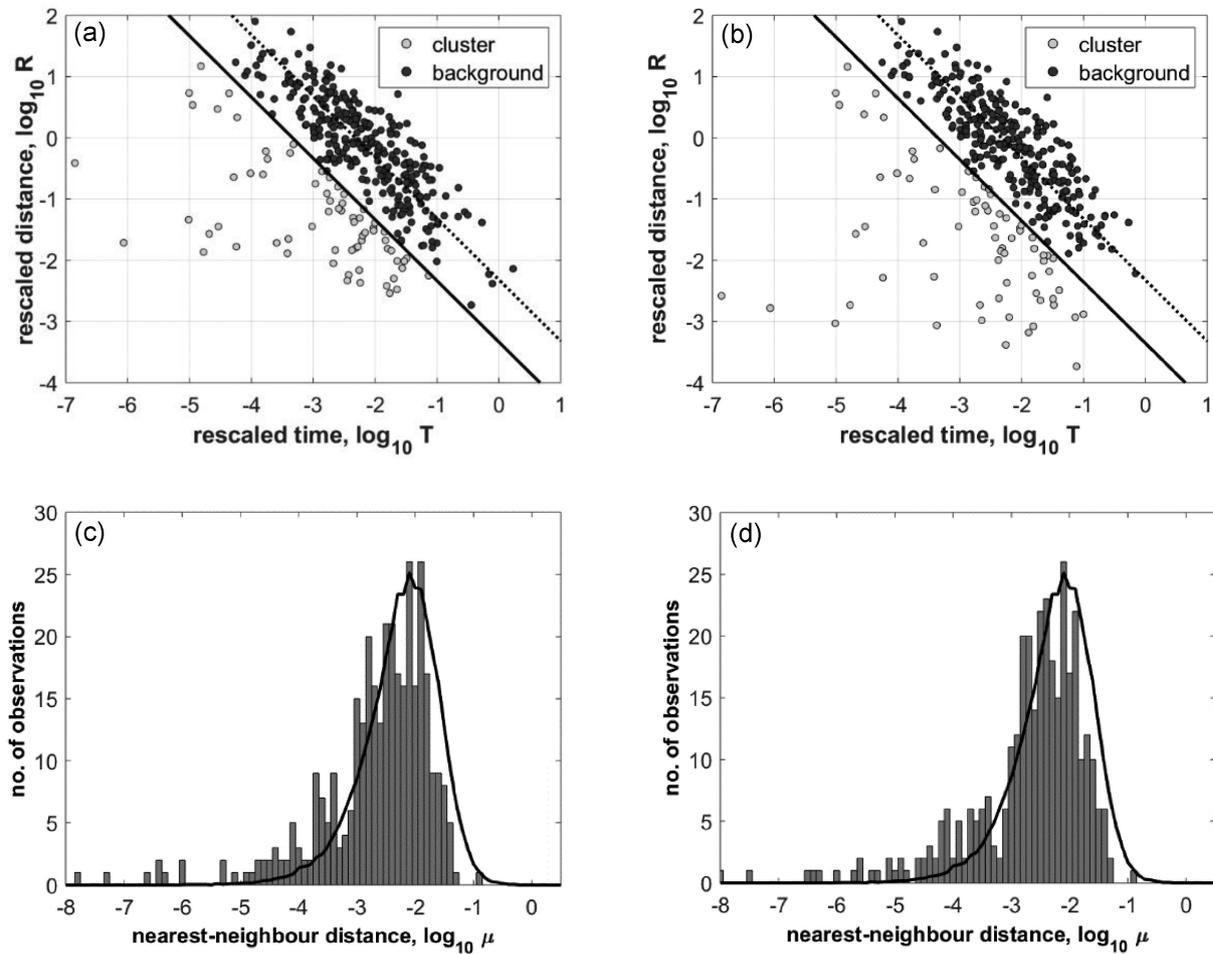
Figure 5. (a–b) Clustering style of seismicity in the Groningen gas field. Each panel shows the 2-D distribution of the rescaled time (T) and rescaled distance (R) to the parent for the Groningen gas field in the period 2015–2019. (c–d) Histogram of the nearest-neighbour distances $\log_{10}\eta_{ij}$ for the Groningen seismicity catalogue. The solid line shows the mean of 100 realizations for a time-stationary, space-inhomogeneous Poisson process with exponential magnitudes. The number of events and inhomogeneous spatial distribution corresponds to the number of events and inhomogeneous spatial distribution of the Groningen relocated seismicity catalogue. (a,c) KNMI catalogue. (b,d) Relocated catalogue of Willacy *et al.* (2019).
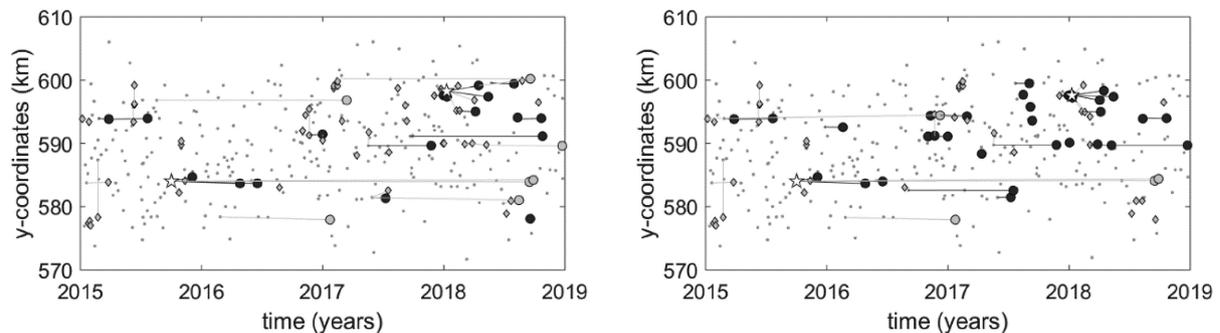
Figure 6. Nearest neighbour forest for events located within one rupture length of its parent. (a) KNMI catalogue. (b) Relocated catalogue of Willacy *et al.* (2019). The stars denote the events of $M \geq 3.0$. The light grey circles indicate the events with $\log_{10}\eta > \log_{10}\eta_0$. The black circles indicate the events with $\log_{10}\eta \leq \log_{10}\eta_0$. For reference, the small grey diamonds indicate events with $\log_{10}\eta \leq \log_{10}\eta_0$ but located further than a single rupture distance of its parent. The stars denote the events of $M \geq 3.0$.

Production induced seismicity can only be explained if the poroelastic deformation of the rock is taken into account. The deformation of the rock induces a change of effective minimum horizontal stress, which is proportional to the pressure change $\Delta\sigma'_h = -\alpha(\frac{v}{1-v})\Delta P$, where α is the Biot–Willis coefficient and v the Poisson's ratio, while the effective vertical stress changes

as $\Delta\sigma'_v = -\alpha\Delta P$. Hence, for fluid extraction the effective vertical stress increases more than the effective minimum horizontal stress, increasing the differential stress for fluid extraction (Fig. 7b) and stress conditions on the faults may shift into the shear-failure regime (Roest & Kuilman 1994; Zoback 2007). Thus the process of inducing seismicity under extraction is much less effective than
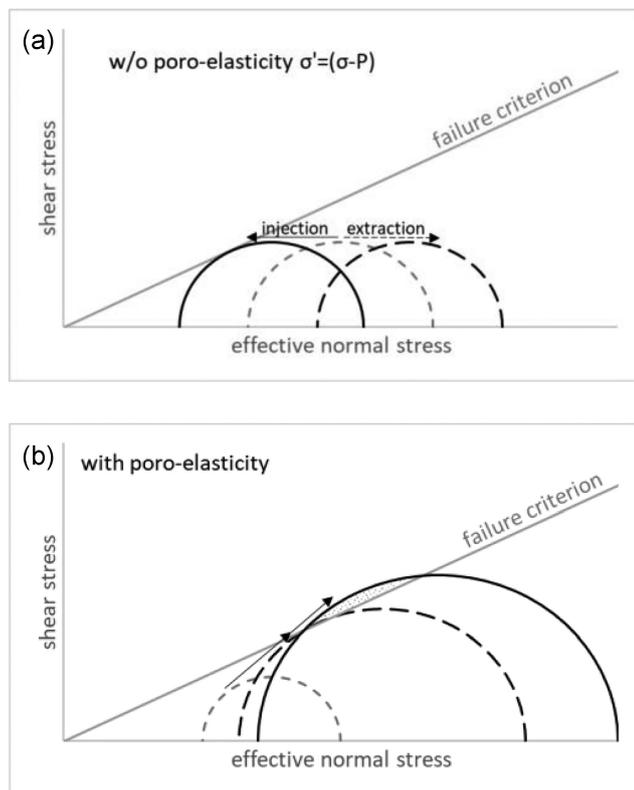
Figure 7. (a) Analysis of effective stress: For injection, the fluid pressure increases in the reservoir and the effective stresses decrease accordingly. The Mohr–Coulomb circle moves to the left towards failure. For extraction, the pore pressure in the reservoir is decreased and the effective stresses increase accordingly. The Mohr–Coulomb circle moves towards the right and no earthquakes will occur. (b) Theory of linear poro-elasticity: Because the horizontal effective stress increases less than the vertical effective stress, the Mohr–Coulomb circle grows and an earthquake can be induced. As the Mohr–Coulomb circle continues to grow with ongoing pressure depletion, ever more faults and fractures at sub-optimal orientations will become critically stressed (dotted area).

the process of inducing injection induced seismicity given the same absolute pressure change.

Given the low background rate, the rate of aftershocks is expected to be significantly reduced as well. The relatively small magnitudes of the Groningen earthquakes further reduce the expected aftershock activity (Ogata 2011).

In line with human induced seismicity in other regions, the imposed continuous loading by gas withdrawal also favours the occurrence of repeaters, characterized by low R and large T values. True repeaters should have very similar waveforms (Jagt *et al.* 2017; Uchida & Bürgmann 2019). Jagt *et al.* (2017) assessed the degree of similarity for Groningen events in the period 2010-mid-2014. In this period they derived six groups of earthquakes representing repeating rupture on the same or nearby faults. Overall, they conclude the data set contains about 10 per cent of repeating events. This is consistent with the percentage of repeaters obtained in this study based on a close proximity in space only.

In addition to the characteristics previously observed, Groningen induced seismicity shows two very distinct characteristics: (1) the presence of a significant number of coincidental events; that is events occurring very close in time to their parent, but situated large distances apart and (2) the presence of a slight abundance
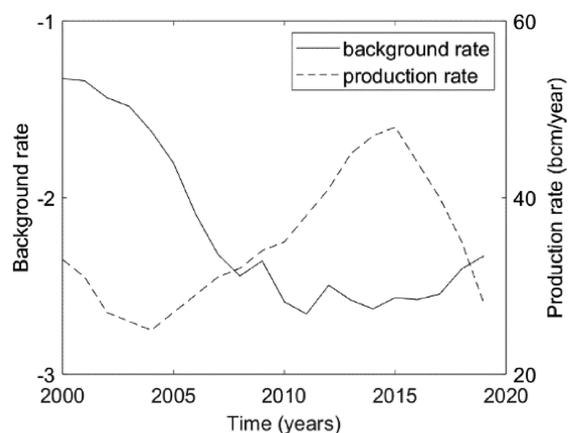
Figure 8. Background and production rates as a function of time. Both were estimated using a 5-yr moving time window. The results are shown at the end of the window; hence the point at 2000 corresponds to the interval (1995–2000), etc.

of events at intermediate nearest neighbour distances ($\log_{10}\eta_0 = -3$ and $\log_{10}\eta_0 = -5$) resulting in a much broader distribution than expected for a time-stationary, space-inhomogeneous Poisson process.

The Groningen gas field is depleted by a large number of wells. The general operational philosophy was to limit pressure differentials over the field. Though the faults within the Groningen gas field may hamper the flow of gas through the reservoir, either by reduced porosity and permeability or due to the increased offset of the reservoir layer, the whole field experiences a relatively even pressure reduction due to the gas withdrawal (NAM 2016, 2017). This means loading of the faults occurs simultaneously throughout the large field. Regionally various local fault patches can be close-to-failure at the same time and induce a sequence of independent events or independent clusters of events within a limited region in a relatively short time frame. In addition, the statistical probability of events occurring very close in time (low T-value), but spatially far apart (large R-value) is significantly larger than in areas of tectonic activity or fluid-injection induced seismicity.

The significant amount of repeaters and coincidental events are mainly responsible for the overabundance of events at intermediate distances. This diffusivity is further enhanced by the rather large location errors of the seismic catalogue which artificially increases the parent-event distances for at least a significant proportion of the non-relocated events. The influence of the non-stationarity of the seismicity rate on the clustering behaviour is found to be minor.

5.2 Gas production and (background) seismicity rates

Several studies have derived a possible correlation between injection/extraction rates and background seismicity rates of human-induced seismicity (Llenos & Michael 2013; Johnson *et al.* 2016; Trugman *et al.* 2016; Martínez-Garzón *et al.* 2018). A similar correlation between the rates of induced seismicity and the rates of gas extraction have been observed for the Groningen gas field (Muntendam-Bos & De Waal 2013; De Waal *et al.* 2015; Nepveu *et al.* 2016; Muntendam-Bos *et al.* 2017; Sijacic *et al.* 2017). Fig. 8 illustrates the dynamics of the background rate and production rate in the period 1995–2019. The analysis is done in a moving window of 5 yr, and the results are shown for the interval (2000–2019);

the first point corresponds to the first full window of 5 yr. The analysis demonstrates that the relation between production rate and background rate is far from straightforward. However, the general observations can be explained conceptually in terms of the perturbations of the regional stress field.

In Groningen, apart from the absence of any (known) tectonic activity, no seismicity was observed for the first 20–25 yr of gas production. This absence of seismicity implies that no fault segments within the Groningen gas field have near-threshold initial stresses at the onset of depletion (Muntendam-Bos & de Waal 2013; Wees *et al.* 2014; Bourne & Oates 2017; Dempsey & Suckale 2017; Candela *et al.* 2018) or the tectonic loading rate is very low, resulting in a very low background seismicity rate (Dieterich 1994; Heimisson 2019). In terms of changes in effective stress, the Mohr–Coulomb circle is far from the failure line, but slowly grows with ongoing pressure depletion (Fig. 7b). During this period changes in loading rates due to changes in gas production rates only result in a slight increase or decrease in the growth-rate of the Mohr–Coulomb circle and hence in a shift of the time necessary for the faults to reach criticality. Changes in loading rate do not influence seismicity rates as no earthquakes can yet occur. Only the absolute level of depletion determines how close faults are to failure and generating earthquakes.

As stresses accumulate by ongoing gas production individual fault patches start to slowly reach close-to-failure stresses. These patches initially occur only very locally, where fault patches are orientated most optimally in the regional stress field (Fig. 7b). Large distances are required statistically to encounter places with near-failure stress values and stress redistribution due to the initial earthquakes is incapable of generating fore-/aftershocks. Hence, the very low but slowly increasing initial seismicity rate and absence of clustered or true fore/aftershock events observed for the period 1995–2003. The sizes of the fault patches that reach criticality may still be small and could also limit the size of the events, explaining the absence of larger magnitude events ($M_L \geq 3$) in this period.

As production in the Groningen gas field continues ever more fault patches obtain close-to-failure stresses (Fig. 7b) and the background seismicity rate between 2004 and 2014 increases further. The increase is mainly driven by the increasing number of fault patches reaching failure. However, the increasing production rate accelerates the growth of the Mohr–Coulomb circle and accelerates the seismicity rate increase (or decrease in background location; Fig. 8). As the fraction of fault segments that are close to failure increases larger magnitude events ($M_L \geq 3$) are generated. As the seismicity rate increases, distances to other near-failure fault patches are reduced and earthquake-related stress redistributions of the larger magnitude events occasionally generate offspring events.

However, the faults in the Groningen gas field are highly irregular in orientation and offset (Visser & Solano Viota 2017). Hence, induced Coulomb stresses are most likely fluctuating and close-to-failure stress still occurs only locally. Stress redistribution of an earthquake may influence the state of stress on nearby patches bringing it closer to failure, but in the absence of near-threshold stress need not produce a response to post-seismic processes. This means the cluster or true fore/aftershock proportion increases, but remains very low. This is further enforced by the relatively small magnitudes of the Groningen earthquakes reducing the expected aftershock activity (Ogata 2011).

As more faults are close to criticality, the statistical probability of generating true fore-/aftershock or clustered events increases. At

the same time, the background seismicity rate becomes more dependent on the loading rate of the faults and hence on the rate of gas production (Dieterich 1994; Heimisson 2019). As a consequence the significant reduction of the gas production rate since 2014 reduced the observed background seismicity rate (represented by an increase in background location in Fig. 8), while the proportion of clustered events remains the same. The reduction in seismicity rate is less pronounced than the reduction in gas production rates, which is due to the fact that stress on the faults keeps increasing with ongoing gas production but at a significantly decelerated rate. Reducing the gas production rate does not decrease the stress on the faults, only slows down the stress increase.

It should be noted that this conceptual explanation is general and based on field wide observations. The overall level of depletion is fairly uniform over the large field, but locally the reduced permeability and offset of the faults have induced pressure differentials of around 1 MPa, especially in the highly active central region. In addition, the reduction of the gas production was initiated by limiting the production from the 5 central clusters by 80 per cent, while increasing production in other parts of the field. This significant change in production strategy has introduced a north–south pressure gradient over the field, where the pressure depletion in the north is currently about 3 MPa less than in the south (on a total depletion of approximately 30 MPa). Muntendam-Bos *et al.* (2017) has shown that as a result the seismicity rate in the centre of the field reduced significantly (the event density reduced by ∼65 per cent from 0.42 events km^{-2} yr^{-1} in 2013 to 0.15 events km^{-2} yr^{-1} in 2015), but the seismicity rate in the southwest of the field, where the production was increased, accelerated (from 0.14 events km^{-2} yr^{-1} in 2013 to 0.24 events km^{-2} yr^{-1} in 2014). Subsequent measures imposed approximately every 6 months over the following few years reduced both the overall production as well as redistributed the production offtake over the field (Muntendam-Bos *et al.* 2017). In the analysis presented here as well as in Muntendam-Bos & De Waal (2013), Nepveu *et al.* 2016 and Sijacic *et al.* (2017) only the cumulative effect of both the production and seismicity rate is assessed. The relatively low seismic activity of the field and the succession of measures imposed impedes a more regional correlation analysis. With the extended network and the concomitant reduction of the magnitude of completeness of the seismic catalogue the analysis might become feasible in the future.

5.3 Implications for declustering induced seismicity catalogues and the derivation of comprehensive seismological models

The results of this study show that the combination of diffuse cluster behaviour with a very low true fore-/aftershock activity renders the ENN-methodology incapable of deriving a proper mode-separation value. The imbalance between the two modes is simply to significant for the Gaussian mixture model to resolve properly. However, this is not unique to this method. Any statistical method aimed at resolving two populations will break down if one of the populations analysed is too small. As a consequence of this breakdown of statistics, a significant proportion of the repeaters, coincidental events and sequences of independent (clusters of) events are erroneously identified as clustered events instead of independent events as the Gaussian mixture model attempts to fit multiple populations. Hence, it is advisable to use caution when applying this methodology to identify fore-/aftershocks sequences or swarms for induced seismicity where the proportion of clustered

events is significantly lower than the proportion of background events.

The analysis presented in this paper does show that some clustered events, occurring at very low nearest neighbour distances, are present in the catalogue. The more in depth analysis of some individual clusters in conjunction with the analysis incorporating the rupture distance of the parent events, confirms that for the Groningen catalogue an assumption of a mode separation value of $\log_{10}\eta_0 = -5$ is reasonable to obtain the proportion of clustered events in the catalogue. Based on this assumption, the actual proportion of background-to-true fore-/aftershock events is estimated at approximately 4 per cent for the period 2015–2019.

Applying the ETAS-model in combination with a seismological model based on an analytical approximation of the Coulomb stresses induced by reservoir depletion to the whole Groningen field, Bourne *et al.* (2018) found an aftershock proportion of 10–15 per cent was required in order to match the observed seismic catalogue. This could indicate this particular seismological model is underestimating the actual seismicity rate induced by the underlying physical process, which is compensated by the ETAS-model. This has major implications for hazard assessments based on model predicted future seismicity rates which also considers the possibility of larger magnitude events (magnitudes 4–6) who, in the overpredicting ETAS-model, will generate a fast overabundance of aftershocks. In fact, given the small proportion of clustering and the general uncertainty in earthquake statistics, the results of this paper indicate that a distinction for earthquake risk modelling in Groningen is unnecessary.

Second order processes such as possible rate-dependence of the seismicity rate could account for the apparent underestimation of the seismological model. This may be attributed to the limited temporal resolution of the model predictions at high frequency due to the annualized approach taken (Bourne *et al.* 2014; Bourne & Oates 2017; Dempsey & Suckale 2017). In doing so, a possible influence of the seasonal swing of the gas production (high production rate during the winter and low production rate during the summer) is missed (Muntendam-Bos & Waal 2013; Nepveu *et al.* 2016; Sijacic *et al.* 2017).

REFERENCES

Ansari, A., Noorzad, A. & Zafarani, H., 2009. Clustering analysis of the seismic catalog of Iran, *Comput. Geosci.,* **35,** 475–486.

Atkinson, G.M. *et al.*, 2016. Hydraulic fracturing and induced seismicity in the Western Canada Sedimentary Basin, *Seismol. Res. Lett.,* **87,** 631–647.

Baiesi, M. & Paczuski, M., 2004. Scale-free networks of earthquakes and aftershocks, *Phys. Rev. E,* **69,** doi:10.1103/PhysRevE.69.066106.

Bao, X. & Eaton, D.W., 2016. Fault activation by hydraulic fracturing in Western Canada, *Science,* **354**(6318), 1406–1409.

Benitez, H.D., Florez, J.F., Duque, D.P., Benavides, A., Baquero, O.L. & Quintero, J., 2013. Spatial pattern recognition of seismic events in South West Colombia, *Comput. Geosci.,* **59,** 60–77.

Bourne, S.J., Oates, S.J., van Elk, J. & Doornhof, D., 2014. A seismological model for earthquakes induced by fluid extraction from a subsurface reservoir, *J. geophys. Res.,* **119,** 8991–9015.

Bourne, S.J., Oates, S.J. & Elk, J., 2018. The exponential rise of induced seismicity with increasing stress levels in the Groningen gas field and its implications for controlling seismic risk, *Geophys. J. Int.,* **213,** 1693–1700.

Bourne, S.J. & Oates, S.J. 2017. Extreme threshold failures within a heterogeneous elastic thin sheet and the spatial-temporal development of induced seismicity within the Groningen gas field, *J. geophys. Res.,* **122,** 10 299–10 320.

Candela, T., Wassing, B., ter Heege, J. & Buijze, L., 2018. How earthquakes are induced, *Science,* **360**(6389), 598–600.

Dieterich, J.H., 1994. A constitutive law for rate of earthquake production and its application to earthquake clustering, *J. geophys. Res.,* **99,** 2601.

Dost, B. & Haak, H., 2007. Natural and Induced seismicity, in *Geology of the Netherlands,* pp. 223–229, eds Wong, Th.E., Batjes, D.A.J. & de Jager, J., Royal Netherlands Academy of Arts and Sciences.

Dost, B. & Kraaijpoel, D., 2013, The August 16, 2012 earthquake near Huizinge (Groningen), Technical report.

Dost, B., Ruigrok, E. & Spetzler, J., 2017. Development of probabilistic hazard assessment for the Groningen gas field, *Neth. J. Geosci.,* **96**(5), s235–s245.

Dempsey, D. & Suckale, J., 2017. Physics-based forecasting of induced seismicity at Groningen gas field, the Netherlands, *Geophys. Res. Lett.,* **44,** 7773–7782.

van Eck, T., Goudbeek, F., Haak, H. & Dost, B., 2006. Seismic hazard due to small-magnitude, shallow-source, induced earthquakes in The Netherlands, *Eng. Geol.,* **87,** 105–121.

van Eijs, R.M.H.E., Mulders, F.M.M., Nepveu, M., Kenter, C. & Scheffers, B.C., 2006. Correlation between hydrocarbon reservoir properties and induced seismicity in The Netherlands, *Eng. Geol.,* **84,** 99–111.

Ellsworth, W.L., 2013. Injection-induced earthquakes, *Science,* **341**(6142), doi:101126/science.1225942.

Freed, A., 2005. Earthquake triggering by static, dynamic, and post-seismic stress transfer, *Ann. Rev. Earth planet. Sci.,* **33,** doi:10.1146/annurev.earth.33.092203.122505.

Georgoulas, G., Konstantaras, A., Katsifarakis, E., Stylios, C.D., Maravelakis, E. & Vachtsevanos, G.J., 2013. "Seismic-mass" density-based algorithm for spatio-temporal clustering, *Expert Syst. Appl.,* **40,** 4183–4189.

Gutenberg, R. & Richter, C.F., 1944. Frequency of earthquakes in California, *Bull. seism. Soc. Am.,* **34**: 185–188

Gutenberg, B & Richter, C.F., 1954. *Seismicity of the Earth and Associated Phenomena,* 2nd edn, Princeton University Press.

Harris, R.A., 1998. Introduction to special section – stress triggers, stress shadows, and implications for seismic hazard, *J. geophys. Res.,* **103,** 24347–24358.

Hartigan, J.A. & Wong, M.A., 1979. Algorithm AS 136: a K-Means clustering algorithm, *J. R. Stat. Soc. C-Appl.,* **28,** 100–108.

Heimisson, E.R., 2019. Constitutive law for earthquake production based on rate-and-state friction: theory and application of interacting sources, *J. geophys. Res.,* **124,** 1802–1821.

Hicks, A., 2011, Clustering in multidimensional spaces with applications to statistical analysis of earthquake clustering, *MSc thesis,* Department of Mathematics and Statistics, University of Nevada, Reno (August 2011).

Jagt, L., Ruigrok, E. & Paulssen, H., 2017. Relocation of clustered earthquakes in the Groningen gas field, *Neth. J. Geosci.,* **96**(5), doi:10.1017/njg.2017.12.

Johnson, C.W., Totten, E.J. & Bürgmann, R., 2016. Depth migration of seasonally induced seismicity at The Geysers geothermal field, *Geophys. Res. Lett.,* **43,** 6196–6204.

Keranen, K.M., Weingarten, M., Abers, G.A., Belkins, B.A. & Ge, S., 2014. Sharp increase in central Oklahoma seismicity since 2008 induced by massive wastewater injection, *Science,* **345,** 448–451.

King, G.C.P., Stein, R.S. & Lin, J., 1994. Static stress changes and the triggering of earthquakes, *Bull. seism. Soc. Am.,* **84**(3), 935–953.

Leonard, M., 2010. Earthquake fault scaling: self-consistent relating of rupture length, width, average displacement, and moment release, *Bull. seism. Soc. Am.,* **100,** 1971–1988.

Leonard, M., 2012. Erratum to Earthquake fault scaling: self-consistent relating of rupture length, width, average displacement, and moment release, *Bull. seism. Soc. Am.,* **102,** 2797.

Llenos, A.L. & Michael, A.J., 2013. Modeling earthquake rate changes in Oklahoma and Arkansas: possible signatures of induced seismicity, *Bull. seism. Soc. Am.,* **103**(5), 2850–2861.

Llenos, A.L. & Michael, A.J., 2016. Characterizing potentially induced earthquake rate changes in the Brawley Seismic Zone, Southern California, *Bull. seism. Soc. Am.,* **106**(5), 2045–2062.

Martínez-Álvarez, F., Gutiérrez-Avilés, D., Morales-Esteban, A., Reyes, J., Amaro-Mellado, J. & Rubio-Escudero, C., 2015. A novel method for seismogenic zoning based on triclustering: application to the Iberian Peninsula, *Entropy,* **17,** 5000–5021.

Martínez-Garzón, P., Zaliapin, I., Ben-Zion, Y., Kwiatek, G. & Bohnhoff, M., 2018. Comparative study of earthquake clustering in relation to hydraulic activities at geothermal fields in California, *J. geophys. Res.,* **123,** 4041–4062.

Monem, M.J. & Hashemy, S.M., 2011. Extracting physical homogeneous regions out of irrigation networks using fuzzy clustering method: a case study for the Ghazvin canal irrigation network, *J. Hydroinform.,* **13,** 652–660.

Mukhopadhyay, B., Fnais, M., Mukhopadhyay, M. & Dasgupta, S., 2010. Seismic cluster analysis for the Burmese-Andaman and West Sunda Arc: insight into subduction kinematics and seismic potentiality, *Geomat. Nat. Hazards Risk,* **1,** 283–314.

Muntendam-Bos, A.G., Roest, J.P.A. & Waal, J.A., 2017. The effect of imposed production measures on gas extraction induced seismic risk, *Neth. J. Geosci.,* **96**(5), s271–s278, doi:10.1017/njg.2017.29.

Muntendam-Bos, A.G., Roest, J.P.A. & de Waal, J.A., 2015. A guideline for assessing seismic risk induced by gas extraction in The Netherlands, *Leading Edge,* **34,** 672–674.

Muntendam-Bos, A.G. & de Waal, J.A., 2013, Reassessment of the probability of higher magnitude earthquakes in the Groningen gas field, Technical report.

Nederlandse Aardolie Maatschappij (NAM), 2016. *Technical Addendum to the Winningsplan Groningen 2016; Production, Subsidence, Induced Earthquakes and Seismic Hazard and Risk Assessment in the Groningen Field,* 57 pp, available at http://www.nam.nl/algemeen/mediatheek-en-downloads/winningsplan-2016.html.

Nederlandse Aardolie Maatschappij (NAM), 2017. *Groningen Dynamic Model Update 2017,* Available at: https://nam-onderzoeksrapporten.data-app.nl/reports/download/groningen/en/d67cb8ac-e5b0-4130-9598-5b7fc83edae2.

Nepveu, M., van Thienen-Visser, K. & Sijacic, D., 2016. Statistics of seismic events at the Groningen field, *Bull. Earthq. Eng.,* **14**(12): 3343–3362.

Ogata, Y., 2011. Significant improvements of the space-time ETAS model for forecasting of accurate baseline seismicity, *Earth Planet Space,* **63**(3), 217–229.

Paleja, R. & Bierman, S., 2016, Measuring changes in earthquake occurrence rates in Groningen, Technical report.

Roest, J.P.A. & Kuilman, W., 1994. Geomechanical analysis of small earthquakesat the Eleveld gas reservoir, in *Conference Proceedings of the Eurock '94. ,* Balkema, pp. 573–580.

Schoenball, M., Davatzes, N.C. & Glen, J.M. G., 2015. Differentiating induced and natural seismicity using space-time-magnitude statistics applied to the Coso geothermal field, *Geophys. Res. Lett.,* **42,** 6221–6228.

Sijacic, D., Pijpers, F., Nepveu, M. & Thienen-Visser, K., 2017. Statistical evidence on the effect of production changes on induced seismicity, *Neth. J. Geosci.,* **96**(5), s27–s38.

Spetzler, J. & Dost, B., 2017. Hypocentre estimation of induced earthquakes in Groningen, *Geophys. J. Int.,* **209,** 453–465.

Stein, R.S., 1999. The role of stress transfer in earthquake occurrence, *Nature,* **402,** 605–609.

Terzaghi, K.V.(1923), Die Berechnung der Durchlässigkeitsziffer des Tones aus dem Verlauf der hydrodynamischen Spannungserscheinungen, Sitzungsber, *Akad. Wiss. Wien, Math.-Naturwiss. Kl., Abt. 2A,* **132,** 125–138.

Toda, S., Lin, J. & Stein, R.S., 2011. Using the 2011 M = 9.0 Tohoku earthquake to test the Coulomb stress triggering hypothesis and to calculate faults brought closer to failure, *Earth Planets Space,* **63,** 1–6.

Trugman, D.T., Shearer, P.M., Borsa, A.A. & Fialko, Y., 2016. A comparison of long-term changes in seismicity at the Geysers, Salton Sea, and Coso geothermal fields, *J. geophys. Res.,* **121,** 225–247.

Uchida, N. & Bürgmann, R., 2019. Repeating earthquakes, *Annu. Rev. Earth planet. Sci.,* **47,** 305–332.

Visser, C.A. & Solano Viota, J.L., 2017. Introduction to the Groningen static reservoir model, *Neth. J. Geosci.,* **96**(5), s39–s46.

de Waal, J.A., Muntendam-Bos, A.G. & Roest, J.P.A., 2015. Production induced subsidence and seismicity in the Groningen gas field – can it be managed? *Proc. IAHS,* **372,** 129–139.

van Wees, J.D., Buijze, L., van Thienen-Visser, K. & Fokker, P.A., 2014. Geomechanics response and induced seismicity during gas field depletion in The Netherlands, *Geothermics,* **52,** 206–219.

Weingarten, M., Ge, S., Godt, J.W., Belkins, B.A. & Rubenstein, J.L., 2015. High-rate injection is associated with the increase in U.S. mid-continent seismicity, *Science,* **348,** 1336–1340.

Willacy, C., van Dedum, E., Minisini, S., Li, J., Blokland, J.W., Das, I. & Droujinine, A., 2019. Full-waveform event location and moment tensor inversion for induced seismicity, *Geophysics,* **84**(2), doi:10.1190/GEO2018-0212.1.

Zaliapin, I., Gabrielov, A., Keilis-Borok, V. & Wong, H., 2008. Clustering analysis of seismicity and aftershock identification, *Phys. Rev. Lett.,* **101,** doi:10.1103/PhysRevLett.101.018501.

Zaliapin, I. & Ben-Zion, Y., 2013. Earthquake clusters in southern California I: identification and stability, *J. geophys. Res.,* **118,** 2847–2864.

Zaliapin, I. & Ben-Zion, Y., 2015. Artefacts of earthquake location errors and short-term incompleteness on seismicity patterns in southern California, *Geophys. J. Int.,* **202,** 1949–1968.

Zaliapin, I. & Ben-Zion, Y., 2016. Discriminating characteristics of tectonic and human-induced seismicity, *Bull. seism. Soc. Am.,* **106**(3), doi:10.1785/0120150211.

Zoback, M., 2007. *Reservoir Geomechanics,* Cambridge Univ. Press.

SUPPORTING INFORMATION

Supplementary data are available at *GJI* online.

Figure S1. 2-D distribution of the rescaled time (T) and rescaled distance (R) to the parent for different parameter variations for the time period 1995–10/2018. (a) Reference scenario, (b) $M_c = 1.5$, (c) fractal dimension d = 1.0, (d) fractal dimension d = 2.0, (e) Gutenberg–Richter b-value $b = 0.8$ and (f) Gutenberg–Richter b-value $b = 1.2$.

Figure S2. Period 1/1995–1/2003: (a) Nearest neighbour forest derived by removing the weak links ($\mu > \mu_0$) from the spanning network. (b) Nearest neighbour forest for events located within one rupture length of its parent. The black circles indicate the events with $\log_{10}\eta \leq \log_{10}\eta_0$.

Figure S3. Period 1/2003–1/2011: (a) Nearest neighbour forest derived by removing the weak links ($\mu > \mu_0$) from the spanning network. (b) Nearest neighbour forest for events located within one rupture length of its parent (grey and black circles). The black circles indicate the events with $\log_{10}\eta \leq \log_{10}\eta_0$.

Figure S4. Period 1/2011–5/2014: (a) Nearest neighbour forest derived by removing the weak links ($\mu > \mu_0$) from the spanning network. (b) Nearest neighbour forest for events located within one rupture length of its parent (grey and black circles). The black circles indicate the events with $\log_{10}\eta \leq \log_{10}\eta_0$.

Figure S5. Period 5/2014–1/2019: (a) Nearest neighbour forest derived by removing the weak links ($\mu > \mu_0$) from the spanning

network. (b) Nearest neighbour forest for events located within one rupture length of its parent (grey and black circles). The black circles indicate the events with $\log_{10} \eta \leq \log_{10} \eta_0$.

Figure S6. (a–d) Histograms of the nearest-neighbour distances $\log_{10} \eta_{ij}$ for the time periods (a) 1995–2003, (b) 2003–2011, (c) 2011–5/2014 and (d) 5/2014–10/2018.

Figure S7. (a) Map of the Groningen gas field and the seismic stations present. The blue squares denote the borehole stations consisting of three-component geophones deployed at four depth levels (50–100–150–200 m) and a surface accelerometer. The orange circles denote the original independent surface accelerometers. (b) Map of the Groningen gas field and its seismicity ($M_l \geq 1.5$) as reported by the Royal Dutch Metrological Institute (KNMI). Shown on the map are the areas containing the individual sequences discussed. The colour coding of the seismicity indicates the local magnitude (-) of the events. (c) Map of the Groningen gas field and all induced seismicity as reported by the Royal Dutch Metrological Institute (KNMI).

Figure S8. (a) Location of the events derived as part of the $M3.1$ Hellum-family. (b) Cluster style of the events derived as part of the $M3.1$ Hellum-family. (c–d) Location and cluster style of the events derived as part of the $M3.4$ Zeerijp-family. (e–f) Location and cluster style of the events of the Wirdum/Loppersum earthquake sequence occurring late 2016, early 2017. The diamonds indicate events which are located at a distance exceeding a single rupture distance of their parent.

Table S1. Basic characteristics of background and cluster populations for the four different parameter assumptions.

Table S2. Event information of the clustered and independent events within the three specific families of events investigated. Events indicated by a star in the depth column are original KNMI catalogue locations.

Please note: Oxford University Press is not responsible for the content or functionality of any supporting materials supplied by the authors. Any queries (other than missing material) should be directed to the corresponding author for the paper.